



The Shadow Knows: Using Shadows to Investigate the Structure of the Pretransitional Disk of HD 100453

Zachary C. Long¹, Rachel B. Fernandes¹, Michael Sitko^{1,2}, Kevin Wagner³, Takayuki Muto⁴, Jun Hashimoto⁵, Katherine Follette^{6,18}, Carol A. Grady⁷, Misato Fukagawa⁸, Yasuhiro Hasegawa^{9,10,11}, Jacques Kluska¹², Stefan Kraus¹², Satoshi Mayama¹³, Michael W. McElwain¹⁴, Daehyon Oh^{5,13}, Motohide Tamura^{5,15,16}, Taichi Uyama¹⁵, John P. Wisniewski¹⁷, and Yi Yang^{5,13}

¹ Department of Physics, University of Cincinnati, Cincinnati, OH 45221, USA

² Center for Extrasolar Planetary Studies, Space Science Institute, 4750 Walnut Street, Suite 205, Boulder, CO 80301, USA

³ Department of Astronomy/Steward Observatory, The University of Arizona, 933 North Cherry Avenue, Tucson, AZ 85721, USA

⁴ Division of Liberal Arts, Kogakuin University, 1-24-2 Nishi-Shinjuku, Shinjuku-ku, Tokyo, 163-8677, Japan

⁵ National Astronomical Observatory of Japan, 2-21-1, Osawa, Mitaka, Tokyo, 181-8588, Japan

⁶ Kavli Institute for Particle Astrophysics and Cosmology, Stanford University, Stanford, CA 94305, USA

⁷ Eureka Scientific, 2452 Delmer Street, Suite 100, Oakland CA 96402, USA

⁸ Division of Particle and Astrophysical Science, Graduate School of Science, Nagoya University, Nagoya, Japan

⁹ Jet Propulsion Laboratory, California Institute of Technology, Pasadena, CA 91109, USA

¹⁰ Institute of Astronomy and Astrophysics, Academia Sinica (ASIAA), Taipei 10641, Taiwan

¹¹ Division of Theoretical Astronomy, National Astronomical Observatory of Japan, Osawa, Mitaka, Tokyo 181-8588, Japan

¹² University of Exeter Astrophysics Group, School of Physics, Stocker Road, Exeter, Devon EX4 4QL, UK

¹³ Department of Astronomical Science, The Graduate University for Advanced Studies (SOKENDAI), Shonan Village, Hayama, Kanagawa 240-0193, Japan

¹⁴ Exoplanets and Stellar Astrophysics Laboratory, Code 667, NASA's Goddard Space Flight Center, Greenbelt, MD 20771, USA

¹⁵ Department of Astronomy and RESCUE, The University of Tokyo, 7-3-1, Hongo, Bunkyo-ku, Tokyo, 113-0033, Japan

¹⁶ Astrobiology Center of NINS, 2-21-1, Osawa, Mitaka, Tokyo, 181-8588, Japan

¹⁷ Homer L. Dodge Department of Physics, University of Oklahoma, Norman, OK 73071, USA

Received 2016 December 27; revised 2017 February 22; accepted 2017 March 2; published 2017 March 24

Abstract

We present Gemini Planet Imager polarized intensity imagery of HD 100453 in Y , J , and $K1$ bands that reveals an inner gap (9–18 au), an outer disk (18–39 au) with two prominent spiral arms, and two azimuthally localized dark features that are also present in Spectro-Polarimetric High-contrast Exoplanet REsearch (SPHERE) total intensity images. Spectral energy distribution fitting further suggests that the radial gap extends to 1 au. The narrow, wedge-like shape of the dark features appears similar to predictions of shadows cast by an inner disk that is misaligned with respect to the outer disk. Using the Monte Carlo radiative transfer code HOCHUNCK3D, we construct a model of the disk that allows us to determine its physical properties in more detail. From the angular separation of the features, we measure the difference in inclination between the disks (45°) and their major axes, PA = 140° east of north for the outer disk, and 100° for the inner disk. We find an outer-disk inclination of $25^\circ \pm 10^\circ$ from face-on, in broad agreement with the Wagner et al. measurement of 34° . SPHERE data in J and H bands indicate a reddish disk, which indicates that HD 100453 is evolving into a young debris disk.

Key words: stars: kinematics and dynamics – planet–disk interactions – polarization – protoplanetary disks – stars: variables: T Tauri, Herbig Ae/Be

1. Introduction

Images of SAO 206462 (Stolker et al. 2016) and HD 142527 (Marino et al. 2015) have revealed azimuthally localized dark features in their outer disks. Both studies interpret the features as shadows cast by an optically thick non-coplanar inner disk. Such an inner disk may be indicative of the existence of planets or large dynamical changes in the disk's history. Modeling of the disk structures can provide a predictive tool for where low-mass companions may be hiding. Sequential follow-up observations can then detect these worlds, as was the case with the young gas giant β Pic b, which, due to its inclined orbit, is driving a similar gravitational warp in the inner disk that was seen before the planet (Apai et al. 2015).

Another disk that exhibits azimuthally localized dark features is associated with HD 100453A (A9V, luminosity $L \sim 9 L_\odot$, mass $M \sim 1.7 M_\odot$ (Dominik et al. 2003), $d = 103 \pm 3$ pc (Gaia Collaboration 2016)), which has an

M4 companion at a separation of $1''.06 \pm 0''.02$ (Chen et al. 2006). Total intensity (TI) imaging at Y - $K2$ bands, obtained by Wagner et al. (2015) with the extreme AO imager Spectro-Polarimetric High-contrast Exoplanet REsearch (SPHERE), revealed two spiral arms, dark features, and the outer extent of the large radial gap inferred from the IR spectral energy distribution (SED) (Maaskant et al. 2013; Khalafinejad et al. 2016).

We present Gemini Planet Imager (GPI) polarized intensity (PI) imagery (Macintosh et al. 2014) of HD 100453. This data set, the SPHERE data, and the infrared SED are modeled using the 3D Monte Carlo radiative transfer code HOCHUNK3D (Whitney et al. 2013). This code allows for two independent and radially separated two-layer disks that need not be coplanar, and the use of multiple grain opacity models. Model images are compared to image data, while simultaneously fitting the SED, to find the cause of the dark features and investigate how structural changes within the disk affect their shape and locations.

¹⁸ NASA Sagan Fellow.

2. Observations and Data Reduction

2.1. GPI Observations and Data Reduction

The source HD 100453 was observed with GPI on 2015 April 10–11 UT using polarimetric differential imaging mode in J , Y , and $K1$ bands. GPI’s “direct” mode uses polarization to suppress stellar light, but not a coronagraphic mask, thereby sacrificing contrast in favor of a tighter inner working angle. We used the shortest exposure time (1.49 s) to minimize saturation and coadded 10 frames to increase the signal-to-noise ratio. The half-wave plate angle was rotated from 0° to 67.5° with 22.5° steps to obtain linear polarization. This sequence was repeated 41, 35, and 36 times, resulting in total exposure time of 41, 35, and 36 minutes for Y , J , and $K1$ bands, respectively. The averaged airmass values were 1.21 and 1.19 in the J and $K1$ bands, respectively.

The data were reduced using the standard polarized data reduction recipe available in GPI pipeline (Maire et al. 2010; Perrin et al. 2014) v. 1.3, with notable customizations. First, microphonics noise was minimized by eye through tuning parameters in the “dstrip science image” primitive. Second, the “subtract mean stellar polarization” primitive was added to the standard polarization recipe to remove instrumental polarization (estimated in the region $1 < r < 10$ pixels, which shows no significant disk emission). Finally, a custom pipeline fix was implemented to allow image alignment in unblocked mode. GPI image alignment typically relies on well-calibrated satellite spots injected by the GPI apodizers that are not present in unblocked mode, therefore a Gaussian stellar centroid was used instead. Although this alignment method is imperfect due to stellar saturation, it worked well in this case. The resulting images were transformed to “radial” Stokes parameters (Schmid et al. 2006). Images used here represent the Q_R component, which holds all linear polarized flux oriented either parallel (negative) or perpendicular (positive) to the line connecting that pixel to the central star. Positive flux in these images therefore represents singly scattered photons from the circumstellar disk.

The system HIP 56071 was observed as a flux standard, with the same procedures, except without closing the AO loop, thereby avoiding saturation. This allowed us to derive conversion factors between $\text{ADU s}^{-1} \text{ pixel}^{-1}$ and mJy asec^{-2} . Since the $K1$ -band magnitude in HIP 56071 was unavailable, we translated the 2MASS K_s -band magnitude into this band by relating the stellar flux to the Vega flux assuming box passbands in two bands (the GPI $K1$ band with $1.9\text{--}2.19 \mu\text{m}$ and the 2MASS K_s band with $1.989\text{--}2.316 \mu\text{m}$) and blackbody radiation with a T_{eff} of 9200 K for HIP 56071 (A1V) and 9700 K for Vega (A0V). The color correction of $K_s\text{ 2MASS} - K1\text{ GPI}$ was -0.002 ; thus, we derived that the $K1\text{ GPI}$ magnitude of HIP 56071 is 7.860. We derived that the conversion factors of $1 \text{ ADU s}^{-1} \text{ pixel}^{-1}$ are 0.846 and $0.853 \text{ mJy asec}^{-2}$ in the J and $K1$ bands, respectively. Note that Y -band flux was not converted into mJy asec^{-2} because no literature value for the Y band is available.

We find the projected separation between the image center and the companion to be $1.''05$, in agreement with Chen et al. (2006). The region within ~ 4 pixels (corresponding to $\sim 0.''06$) from the central star is saturated. We conservatively estimate the features outside 6–7 pixels from the center to be real, while the area interior to this radius is washed out by speckle residuals. We detect the outer disk and spirals, as in Wagner et al. (2015). The total PI within $0.''1 < r < 1.''0$ (the inner radius corresponds to 7 pixels) is 13 and 22 mJy for J and $K1$ bands, respectively.

2.2. Archival Total Intensity Imagery and Assembly of the IR SED

Wagner et al. (2015) also observed HD 100453 with VLT/SPHERE on 2015 April 10. The observations were carried out in IRDIFS extended mode¹⁹ (Girard et al. 2016) using IRDIS to take dual-band TI images in $K1$ and $K2$ bands and simultaneously using the IFS to obtain low-resolution spectra from Y to H bands. Data reduction is described in Wagner et al. (2015). Photometry used in constructing the SED of HD 100453 includes all sources mentioned in Khalafinejad et al. (2016) as well as *Herschel* PACS data at 70, 100, and $160 \mu\text{m}$ (Pascual et al. 2015), and 2MASS at J , H , and K_s bands (Cutri et al. 2003).

3. Results

3.1. SPHERE and GPI Imagery

A radial gap can clearly be seen from $9 \pm 2 \text{ au}$, to $18 \pm 2 \text{ au}$ in the GPI imagery (Figure 1). Inside 9 au the GPI image is saturated, making the inner edge of the gap inaccessible in the image. The outer radius agrees with the Wagner et al. (2015) estimate of $\sim 19 \text{ au}$ using $d = 103 \pm 3 \text{ pc}$ (Gaia Collaboration 2016), and the Khalafinejad et al. (2016) estimate of $20 \pm 2 \text{ au}$ from SED modeling. We measure a pericenter offset upper limit of 1 ± 1 pixels ($0.''014 \pm 0.''014$) (Figure 1).

The outer disk is brightest on the southern side in both PI and TI imagery, implying that this is the near side of the disk. However, the northern spiral arm is brighter in PI images while the southern arm is brighter in TI images, indicating possible differences in grain properties. Additionally, there is a dropoff in the spiral arm intensity at longer wavelengths in SPHERE TI images, which suggests that they are made of smaller grains than the outer disk. After absolute flux calibration of the TI images using archival 2MASS photometry (Cutri et al. 2003), we measure the total TI flux between $0.''1 < r < 1.''0$ is 49 mJy and 70 mJy in J and H bands, respectively. Using this and the 2MASS flux, we calculate a fractional luminosity for the outer disk $\frac{f_{\text{disk}}}{f_{\text{total}}}$ of 0.018 ± 0.001 for J band and 0.025 ± 0.002 for H band, which may suggest that the outer disk is reddish and therefore comprised of large compact grains (Mulders et al. 2013). By contrast, we calculate a fractional luminosity for the spiral arms of 0.0040 ± 0.001 for J band and 0.0045 ± 0.001 for H band, which, although slightly red, is more blue than the rest of the outer disk. This indicates that they may be comprised of smaller grains (Mulders et al. 2013).

Two distinct azimuthally localized dark features are seen at the same position angle (PA) in both TI and PI images, and they are therefore not artifacts of PI imagery. They also have a similar contrast of outer disk to feature in all available bands (Figure 1).

3.2. Determining the Likely Cause of the Dark Features

We discuss three possible physical scenarios for the origin of the dark features: a physical gap due to the dynamical clearing of a large body, grain growth and settling, or shadows cast from an inner-disk component.

The SPHERE Y band point-spread function (PSF) for HD 100453A has a FWHM of 5 pixels (3.8 au). This suggests that the dark features are resolved and have an azimuthal extent of 14 ± 2 pixels ($10 \pm 1.5 \text{ au}$) based on the FWHM of the

¹⁹ Very Large Telescope SPHERE User Manual.

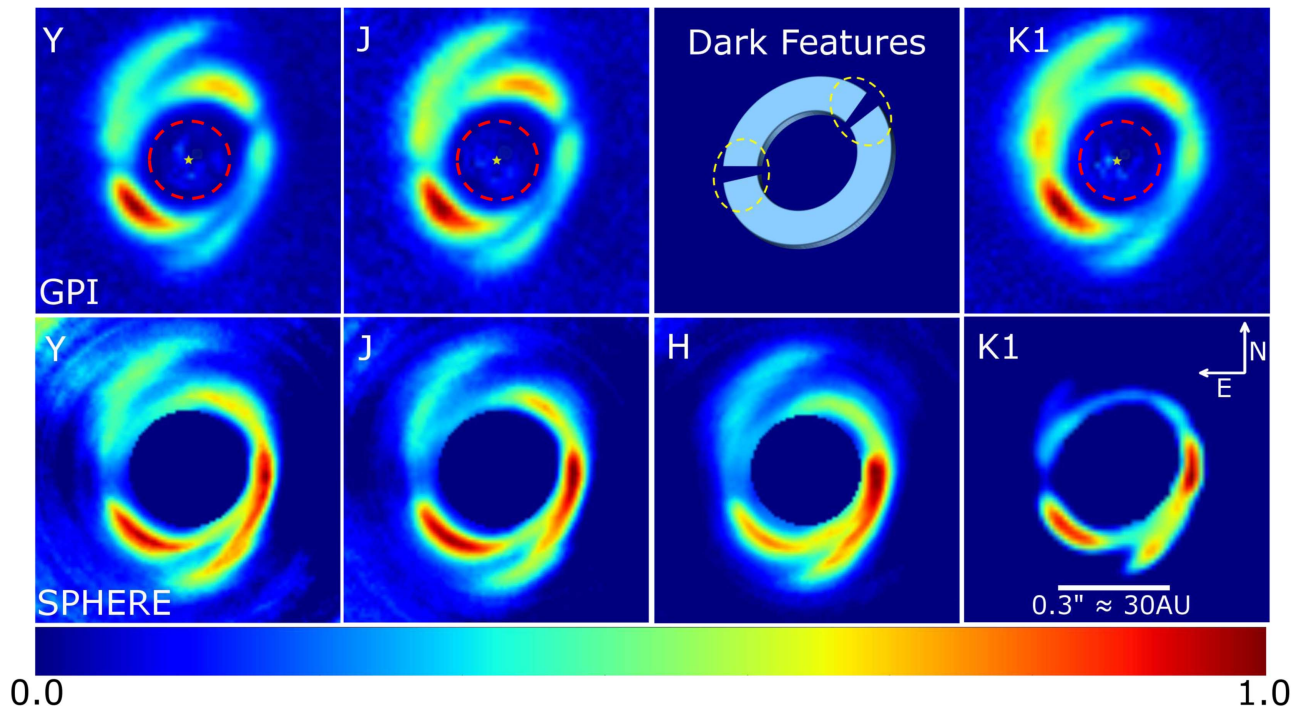


Figure 1. r^2 -scaled GPI polarized intensity images in Y , J , and $K1$ bands, plus a schematic of the disk marking the locations of the dark features (top row), and r^2 -scaled SPHERE total intensity images of HD 100453 in Y , J , H , and $K1$ bands (bottom row). The images have a field of view of $0''.8 \times 0''.8$ and are normalized by the maximum intensity in each band. The central star is represented by a yellow star in GPI images, and the inner working angle is represented by a red dashed line.

eastern feature in this image. If the dark feature is due to the clearing of a single body's Hill sphere (Hamilton & Burns 1992), it would correspond to an M-type star with a mass of at least $0.4 M_{\odot}$. The M-type companion, HD 100453B, is visible in SPHERE, GPI, and *Chandra* (Collins et al. 2009) imagery. An M-type star with a mass of $0.4 M_{\odot}$ therefore would certainly be visible in the location of the dark features if it existed. Thus, we reject the hypothesis of local clearing to explain the dark features.

Grain growth and settling has been suggested as a source of dark regions at near-IR (NIR) wavelengths (Dullemond & Dominik 2004a, 2004b; Bimstiel et al. 2012) and should also produce bright rings in the submillimeter. This would require a resolution of at least $0''.03$, which is reachable by interferometric telescopes such as ALMA. The differential rotation of the disk would cause the dark features to deform over time, however, which suggests that grain growth and settling is not the cause of the features.

An inner disk would cast two shadows that have a large radial extent and have a similar contrast of the outer disk to the shadow over the wavelength range in which it is optically thick (Stolker et al. 2016), similar to what is seen in the GPI and SPHERE images. We show that shadows cast by an inner disk with a suitable inclination are fully capable of producing such dark features. In the following sections we present a model that is capable of generating the dark features as well as reproducing the observed SED.

3.3. Development of Preliminary Model

3.3.1. Literature Values for the Outer-disk Inclination

Fung & Dong (2015) adopted $i \sim 5^{\circ}$, where i is the outer-disk inclination from face on with respect to the observer, to reproduce the spiral arm morphology in hydrostatic modeling of the HD

100453 system. If we accept the Fung & Dong (2015) assumption of a completely coplanar disk, we can also assume the equatorial plane of the star is coplanar because according to Greaves et al. (2014), most stars rotate in the same plane as their disks. Using the 5° inclination for the outer disk and a $v \sin i$ of $48 \pm 2 \text{ km s}^{-1}$ for HD 100453A (Guimarães et al. 2006), we find that the equatorial velocity of HD 100453A would be $\sim 550 \text{ km s}^{-1}$, which is 150 km s^{-1} above the break-up velocity of the star (Slettebak 1966). Because HD 100453A is still intact, a 5° inclination for the star is non-physical, which implies by extension that the inclination of the outer disk cannot be 5° either. Moreover, in GPI images we can clearly see the major and minor axes of the disk, which would not be possible given a nearly face-on disk as in TW Hydrae (Andrews et al. 2016). If the spiral arms are close to face on, as Fung & Dong (2015) suggest, they are not coplanar with the outer disk.

Wagner et al. (2015) measured an outer-disk inclination of $i \sim 34^{\circ}$ from face on through fitting an ellipse to the peak intensity along the center of the outer disk and assuming circular geometry. However, because the outer disk has finite thickness, this method will overestimate the outer disk's inclination. We review this inclination in Section 3.3.3.

3.3.2. Initial Modeling Parameters

In order to reduce the degeneracies in our model, literature values, SPHERE and GPI imagery, and the SED (Figure 2) are used in combination to determine the initial modeling parameters. For the star we used a PHOENIX stellar atmosphere model (Brott & Hauschildt 2005) with $T = 7400 \text{ K}$ (appropriate for an A9 star) and a distance of 103 pc (Gaia Collaboration 2016). HOCHUNK3D uses the Lucy (1999) method for calculating temperature in our model. Box filters were created in Y - $K2$ to allow for a direct comparison of the model to data.

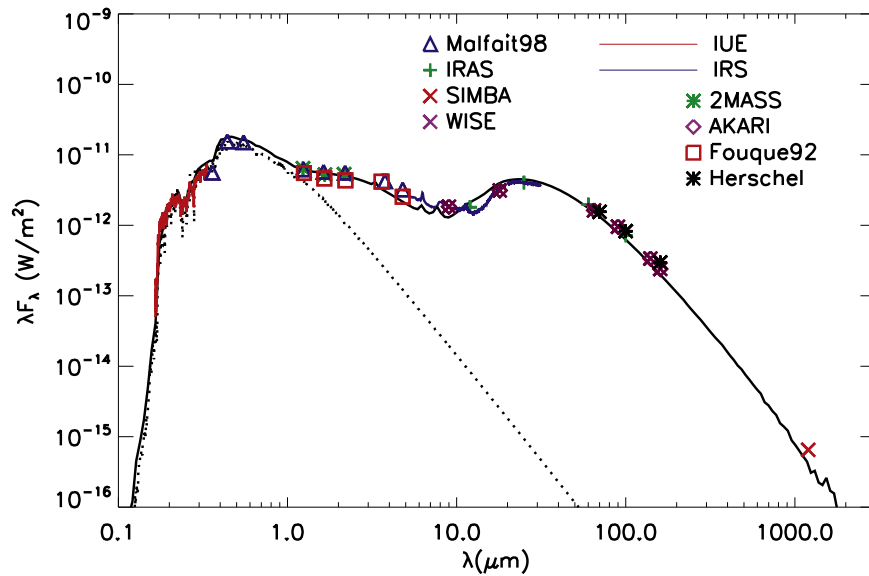


Figure 2. Best model fit (solid line) of the SED of HD 100453 after initial modeling, with the stellar atmosphere (dotted line) visible as well.

Through SED fitting, Khalafinejad et al. (2016) suggested that the inner disk extends from 0.25 to 1.7 au. Confirmation of the inner edge radius is provided by H -band interferometry with VLTI/PIONIER (Lazareff et al. 2017), which find an upper limit of 0.27 au. The inner disk extends to at least 0.9 ± 0.1 au from the N -band half-light radius of VLTI/MIDI (Menu et al. 2015), updated using $d = 103 \pm 3$ pc (Gaia Collaboration 2016). The long-wavelength slope obtained from the 1.2 mm SIMBA point (Meeus et al. 2002b), the reddish color of the outer disk (Section 3.1), and the lack of a strong silicate peak in the SED (Meeus et al. 2002a) imply that the inner and outer disks are comprised of large compact dust grains (Mulders et al. 2013).

To match these dust properties, we used Model 2 from Wood et al. (2002) for the settled disk grain opacities. This contains a mixture of amorphous carbon and astronomical silicates, a radial power-law exponent (a) of 3.5 for both grain compositions, no exponential cutoff to the grain size distribution, a maximum particle size ≤ 1 mm, and a minimum particle size of $0.01 \mu\text{m}$. For the less-settled grain opacities we used Model 1 from Wood et al. (2002). Similarly, this contains a mixture of amorphous carbon and astronomical silicates, a power-law size distribution with $a = 3.5$ and 3.0 , respectively, plus an exponential cutoff with a turnover at $50 \mu\text{m}$, a maximum particle size ≤ 1 mm, and a minimum particle size of $0.01 \mu\text{m}$.

3.3.3. Inclination of the Outer Disk

Because reproducing the spiral arms is not necessary for studying the cause of the dark features, they are not included in our models. We calculated models with $5^\circ \leq i \leq 45^\circ$ in 5° increments and compared the resulting model images to observed images; we find a best fit of $25^\circ \pm 10^\circ$. From this model we also find a PA for the outer disk’s major axis of $140^\circ \pm 10^\circ$ east of north.

3.4. Adopted Model Parameters

After initial modeling of the outer disk, we constructed a more complete disk model to fit the SED (Figure 2). We find that our model closely matches the observed SED, including the NIR

region, which was ignored by Bensity et al. (2017), to be discussed later. It consists of an inner disk ($\sim 0.13\text{--}1 \pm 0.5$ au), which reproduces the IR excess of the SED and is in agreement with VLTI/MIDI measurements of 0.9 ± 0.1 au. This is followed by a depleted region to 18 au, and finally, by an outer disk (18–39 au). The inner disk has a vertical inner-edge thickness of 0.11 ± 0.05 au as defined by $z = Cr^b$, where z is the density scale height (thickness) of the disk, C is a constant, r is the radial distance from the star, and b is the flaring exponent (Whitney et al. 2003). To match mid- to far-IR emission, we find $b = 1.28 \pm 0.02$, which falls within the canonical values of 1.25–1.3 for irradiated disks (Chiang & Goldreich 1997; Hartmann et al. 1998). Changes in the settled disk have little effect on the SED and were not changed appreciably in our modeling. Our final parameters for the settled disk were $z = 0.0004$ au and $b = 1.25$. Both the vertical density and the surface density profile are as described in Whitney et al. (2013) for a disk in hydrostatic equilibrium. In particular, we chose density exponents $\alpha = 2.30$ and $\alpha = 2.25$ for the less settled and the settled disks, respectively.

3.5. Difference in Inclination for the Inner Disk

3.5.1. Definition of Δi

In this section we test the validity of a difference in inclination between the inner and outer disk as the cause of the dark features. We define this difference in inclination as $\Delta i = i - \beta$, where i is the inclination of the outer disk from face on and β is the inclination of the inner disk from face on. While we define i as positive, β can be positive or negative, depending on the direction of tilt of the inner disk (Figure 3).

3.5.2. Azimuthal Separation of Dark Features and Comparison to Model

Model images were produced with the adopted $i = 25^\circ$, while Δi was varied in 10° increments from 0° to 70° (Figure 4). These were convolved with the PSF of SPHERE J -band images and therefore produced clearer shadows than longer wavelength bands. No azimuthally localized dark features were observed in

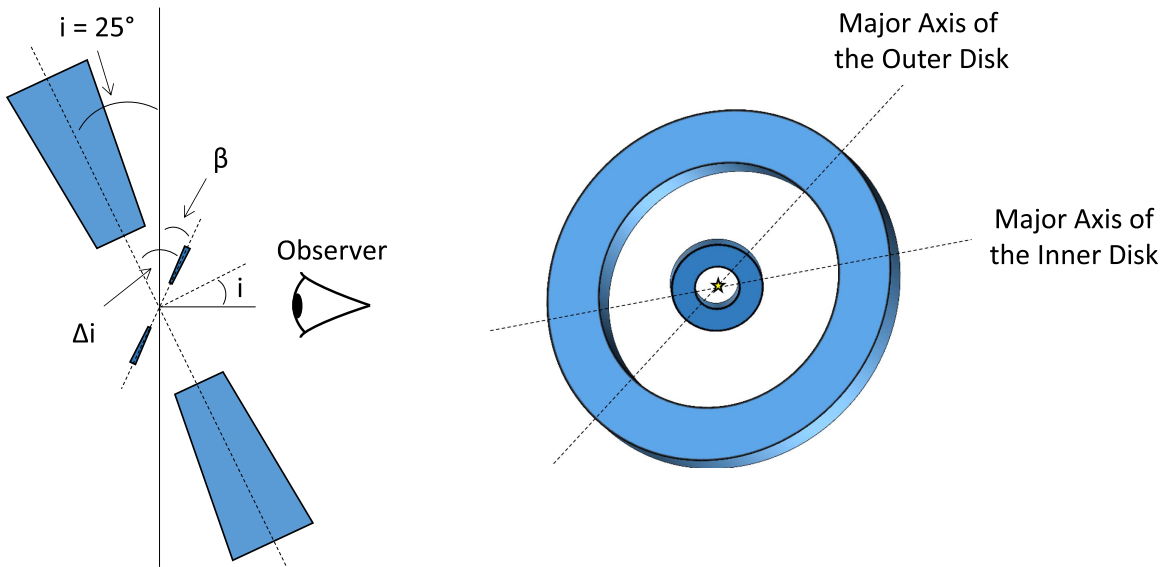


Figure 3. Left: cross section of the disk structure with $\Delta i = i - \beta$, where i is the positive inclination of the outer disk from face on with respect to the observer, while β is the positive or negative inclination of the inner disk from face on. Right: schematic view of the overall disk structure of HD 100453 in the observed frame, as deduced from our best-fit model (Section 3). The major axes of the inner and outer disks are marked.

model images with $\Delta i = 0^\circ$ despite a good fit to the SED, excluding a coplanar disk system. At $\Delta i = 20^\circ$, the inner-disk shadows the northern section of the image and predicts too much flux between 1 and $10 \mu\text{m}$ because of its nearly face-on orientation with respect to the observer (Figure 4). Moving to $\Delta i = 70^\circ$, the shadows narrow and predict too little flux between 1 and $10 \mu\text{m}$ because the inner disk is nearly edge-on to the observer. We find that $\Delta i = 45^\circ \pm 10^\circ$ matches the general appearance of the imagery, to be quantified below.

Azimuthal intensity profiles of the GPI images and model imagery were generated for the outer disk (Figure 5) and measure an azimuthal separation of $140^\circ \pm 10^\circ$ for the dark features, which are in the same locations in each band. The additional local minimum in intensity profile plots is due to polarization effects along the minor axis of the outer disk. We find that as Δi is increased, the shadow separation also increases and produces a best fit to the dark features at $\Delta i = 45^\circ \pm 10^\circ$, which corresponds to $\beta = -20^\circ \pm 10^\circ$. This deduced inner-disk inclination angle is significantly different from the angle found in Lazareff et al. (2017), $\beta = -48^\circ$, using H -band interferometry with VLT/PIONIER. The main source of uncertainty in our measurement comes from the azimuthal extent of the shadowed region. To match the dark features' azimuthal location, we rotated the inner disk by -40° with respect to the outer disk, which places the major axis of the inner disk at $100^\circ \pm 10^\circ$ east of north. This differs from the PA for the major axis found in Lazareff et al. (2017), 81° , and is discussed later.

A recent study by Benisty et al. (2017) also proposed a misaligned inner disk as the cause of the outer disk shadowing in HD 100453. The authors generate a model to test this hypothesis using measurements from Lazareff et al. (2017). In order to test the validity of their model, we generated our own using their value for the outer-disk inclination, $i = 38^\circ$, and their quoted Δi of 72° . This model does not produce shadows in the same locations as in the data (Figure 6), however, similar to what was found earlier in this section.

In our modeling we find that the inclination of the outer disk had little effect on the separation of the shadows on its own, unless the near side of the outer disk is reversed. We also find that the separation of the shadows is smaller than 180° on the side of the outer disk, which corresponds to the near side of the inner disk. Essentially, the inner-disk major axis divides the outer disk into two semicircles. The 180° constraint implies that the centers of the shadows cannot exist in separate semicircles, and this strongly constrains the orientation of the inner disk. In Figure 6 we see that the quoted orientation of the inner-disk major axis places the shadows in separate semicircles in the GPI image, which cannot occur if the inner disk is the source of the shadows. In addition, the gap has a visibly more strongly elliptical structure in the Benisty et al. (2017) model than in the data, which is most likely due to the thickness of the outer disk, as discussed in Section 3.4, as well as to the larger inclination of the outer disk. It is important to note that this Δi corresponds to $\beta = -34^\circ$ instead of the inner-disk inclination proposed separately in Benisty et al. (2017) of $\beta = -48^\circ$. Additionally, in our modeling we find that the NIR region of the SED is fairly sensitive to the inclination of the inner disk (Figure 4). Because Benisty et al. (2017) did not fit the NIR excess of the SED, the Benisty et al. (2017) model is not as tightly constrained as our simultaneous image and SED fitting. We found the inclination of the inner disk proposed by Benisty et al. (2017) did not produce a good match to the 1–10 micron SED nor the constraints on the shadows that we found (Figure 7). Differences in the inner disk orientation which produce shadows along an axis other than the major axis may be possible, though we did not observe this in the parameter space of our modeling.

3.6. Effects of Inner-disk Thickness and Outer-disk Flaring on Shadows

To examine how the inner-disk thickness affects the morphology of the shadows, we generated model images at inner-edge inner-disk thicknesses from 0.07 to 0.14 au in increments of

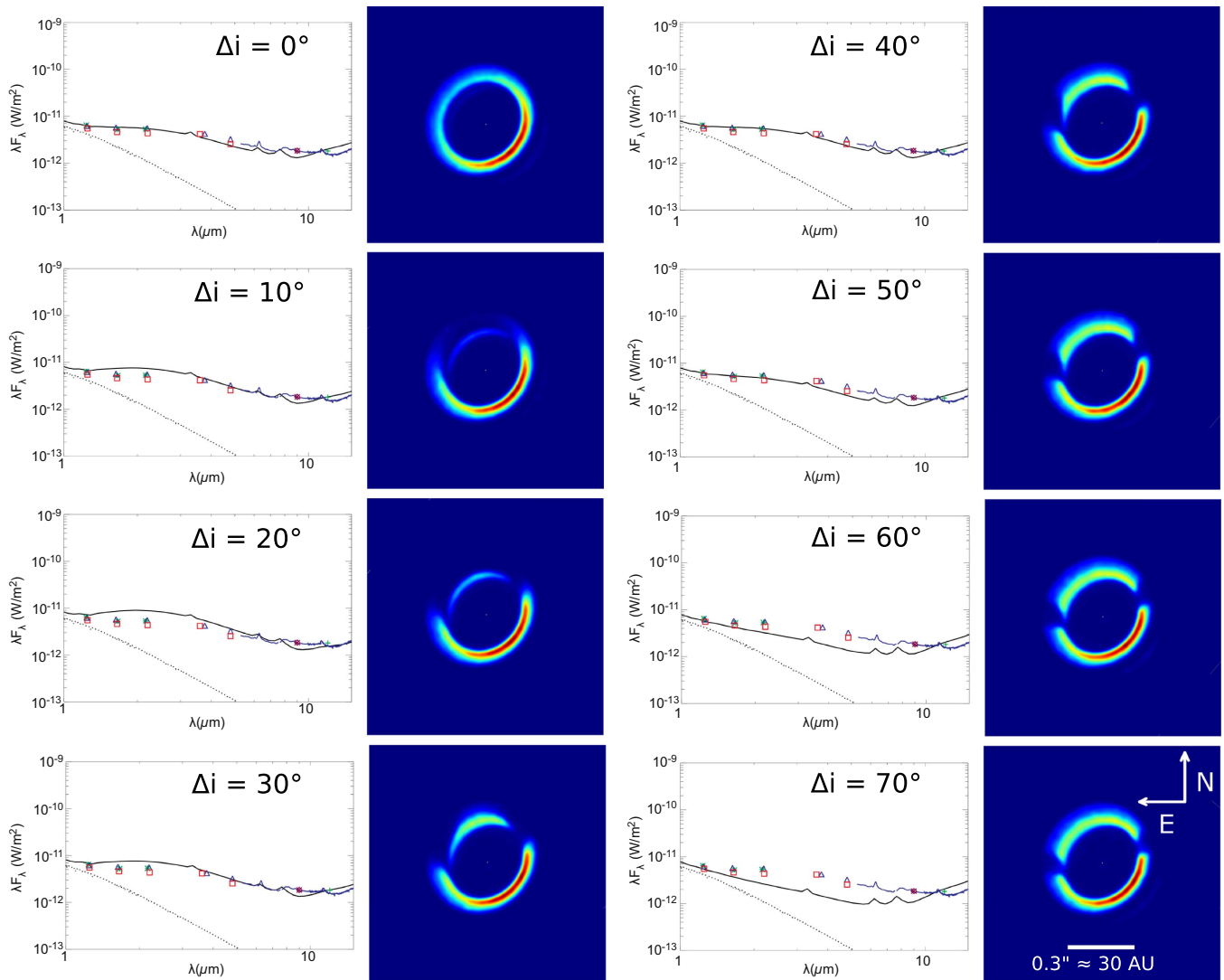


Figure 4. SEDs between 1 and 10 μm coupled with r^2 -scaled total intensity model images at J band, convolved with the PSF of SPHERE total intensity imagery of various Δi . Here the $\Delta i = 0$ does not produce dark features, and therefore HD 100453 cannot have two coplanar disks. We find a best fit of $\Delta i = 45^\circ \pm 10^\circ$.

0.014 au without fitting the SED. We find that as the thickness increases, the width of the shadows increases with no change in the location of the shadows. (Figure 8). The differences in width become small at smaller thicknesses, however, suggesting that shadows can act as an upper constraint of the inner-disk thickness.

Model images were also generated at flaring exponents (Section 3.4) of 1.00, 1.20, and 1.40 (Figure 9) in order to examine the effect of the outer-disk structure on shadow morphology, also without fitting the SED. We find that the width of the shadows' inner edge decreases with increasing b , while the outer edge remains largely unaffected. In addition, we observe that the flaring of the disk causes the outer disk to appear thicker on the far side, as seen in Figure 9, where the SW side is the near side of the outer disk. This effect is most prevalent in the rightmost panel, where the SW side of the disk is approximately half the thickness of the NE side. In the case of HD 100453, the SW side of the outer disk is narrower in GPI images (Figure 1), indicating that this is the near side. The ratio of thicknesses between the near and far side of the disk, coupled with the inclination of the outer disk, could allow us to quantitatively

describe the degree of flaring of the outer disk. When taken in conjunction with the inner-disk thickness, this should allow us to strongly constrain the disk's physical structure.

3.7. Using Shadows to Determine the Near Side of the Inner and Outer Disk

As a result of the thickness of the outer disk, we find that any $\Delta i \neq |90^\circ|$ will offset the apparent location of the shadows on the outer disk in the direction of the tilt of the inner disk (Figure 10). The shadows are cast along the major axis of the inner disk and create a shadow, which is not coplanar with the outer disk, on the inner edge of the outer disk. The shadow will therefore be shifted by an amount that depends both on the thickness of the outer disk and on the value of Δi . This suggests that the separation of shadows must be smaller than 180° on the side of the outer disk, which corresponds to the near side of the inner disk, as seen in Figure 10. Examination of the shadow location therefore allows for a simple effective method of determining the near side of the inner disk. In the

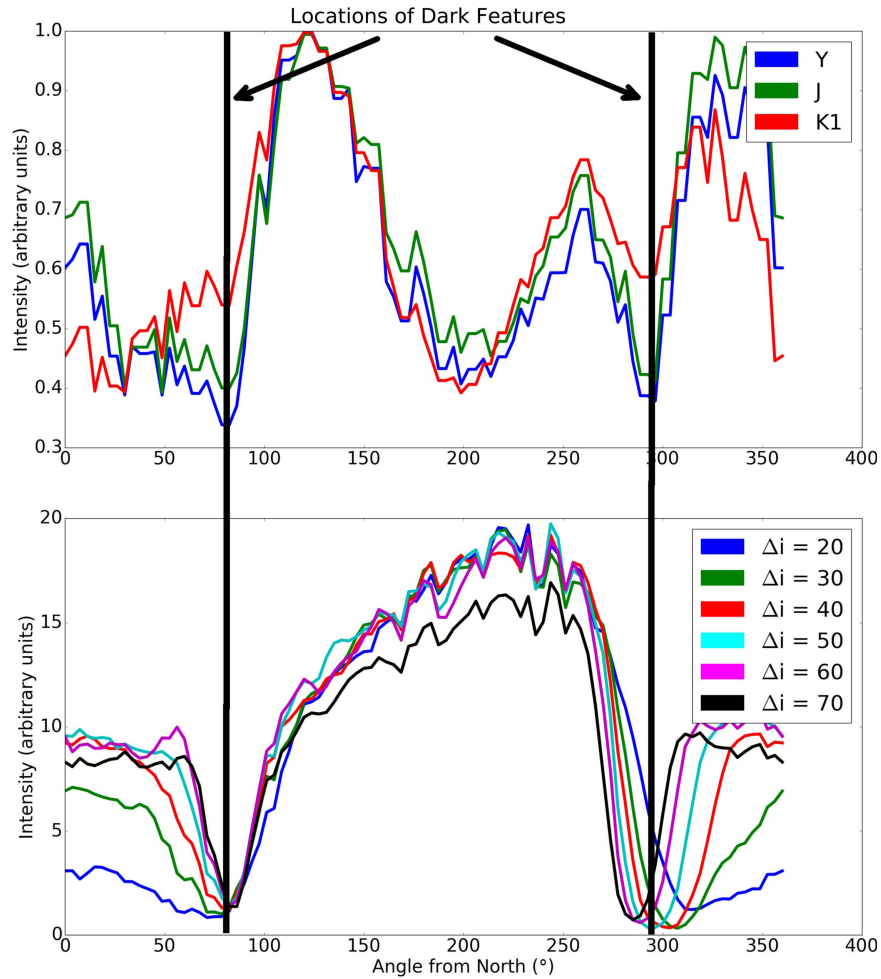


Figure 5. Colored lines represent azimuthal intensity profiles of GPI polarized intensity (top) and total intensity J -band model (bottom) images where 0° represents due north, and we trace counterclockwise along the outer disk. GPI traces are normalized by the maximum intensity in each band. Model images are convolved with the PSF of SPHERE imagery and unscaled. The vertical black lines mark the position of the dark features.

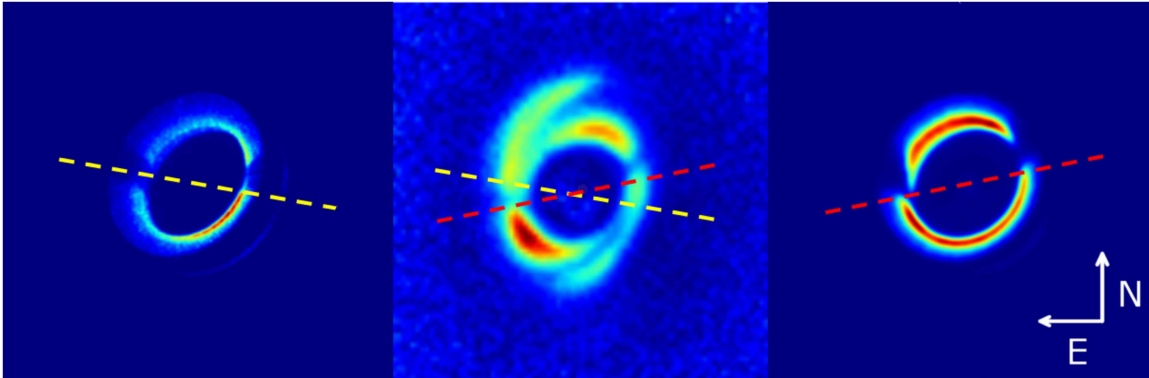


Figure 6. Left: r^2 -scaled total intensity model recreation of Bessy et al. (2017) at J band, convolved with the PSF of SPHERE total intensity imagery. Center: observational GPI polarized intensity r^2 -scaled J -band image. Right: r^2 -scaled total intensity model image at J band of our best-fit model outlined in Section 3.5, convolved with the J -band PSF of SPHERE total intensity image. Here, the yellow dotted line shows the major axis PA of the inner disk in the model recreation of Bessy et al. (2017), and the red dotted line represents the major axis PA of the inner disk in our model. It is apparent from the figure that in the model recreation of Bessy et al. (2017) neither the major axis location nor the shadow locations themselves match the locations of the shadows in the data. In addition, simple visual examination of this model reveals that both the azimuthal separation of the shadows and the ellipticity are too large to match the observational data.

case of HD 100453, it is clear that the northern side of the inner disk is the near side because the shadow separation is smaller than 180° on that side. In contrast, it is much more difficult to discern the near side of the outer disk via examination of the shadows because this depends on both the tilt of the outer disk

and Δi . In this case, because we know $\Delta i = 45^\circ$, the inclination of the outer disk is $|25^\circ|$ from Section 3.3.3, and from the NIR portion of the SED we are not looking along the edge of the inner disk, the SW side of the disk must be the near side.

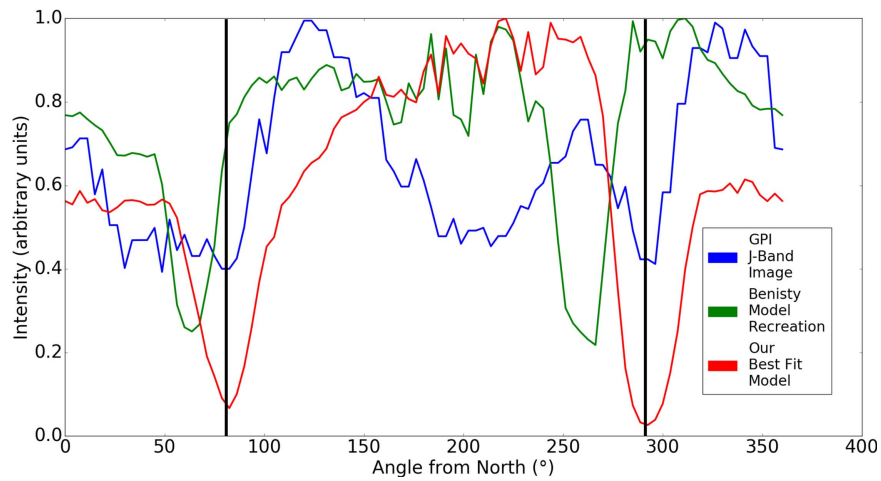


Figure 7. Colored lines represent azimuthal profiles of GPI polarized intensity, our best-fit *J*-band model, and our recreation of the Bensity et al. (2017) model. The vertical black lines represent the location of the shadows in the GPI image. In our model recreation with $\Delta i = 72^\circ$ and $i = 38^\circ$, neither the location of the shadows nor their separation agree with the GPI imagery.

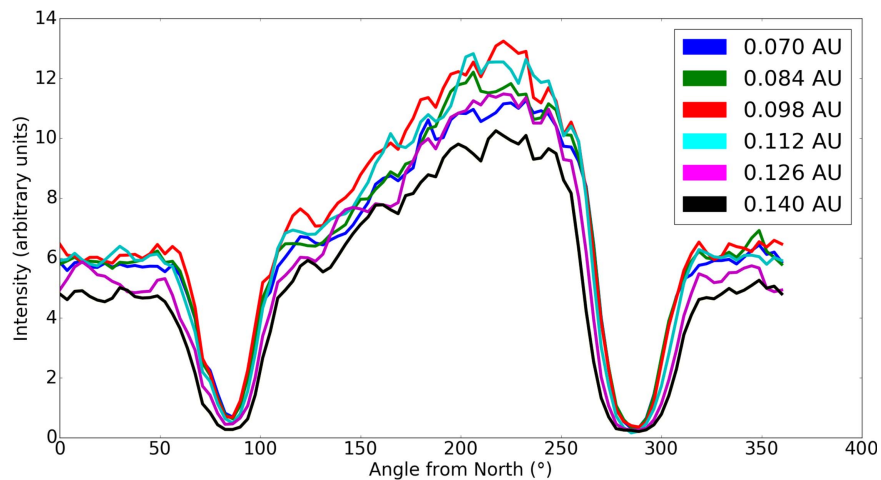


Figure 8. Graph showing the effects of inner-disk thickness on the width of the dark features. The colored lines represent intensity traces derived from unscaled *J*-band total intensity model images convolved with the PSF of SPHERE total intensity imagery. 0° represents due north, and we trace counterclockwise along the outer disk. We find that as the thickness increases, the width of the dips associated with the shadows also increases, while their intensity decreases.

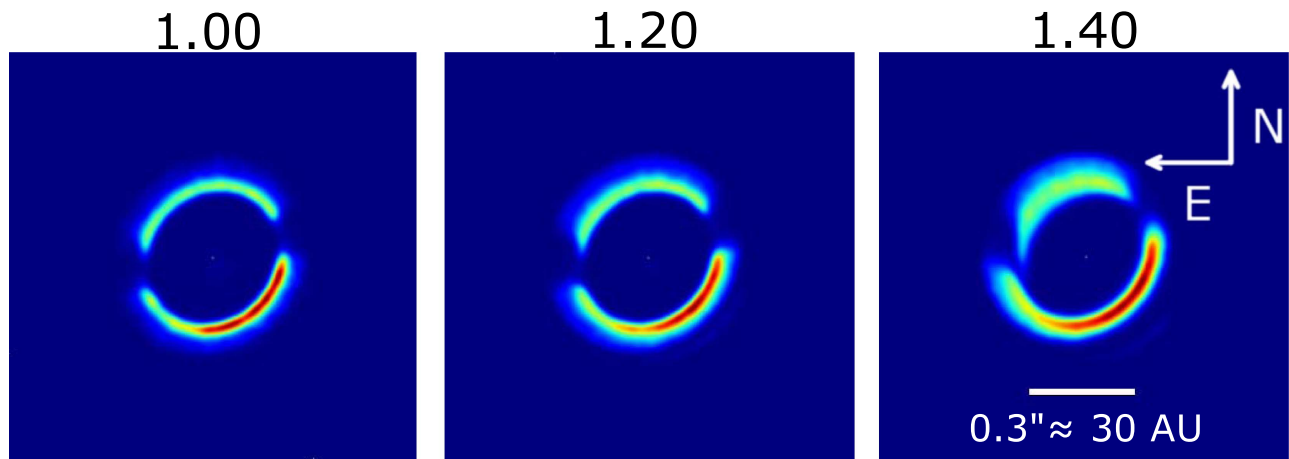


Figure 9. Figures showing the images generated through the total intensity model at *J* band with flaring exponents (Section 3.4) of 1.00, 1.20, and 1.40. Model images are convolved with the PSF of SPHERE imagery and unscaled. The SW side is the near side of the outer disk, and it is clear that the near edge is thinner in the flared disks than the far edge.

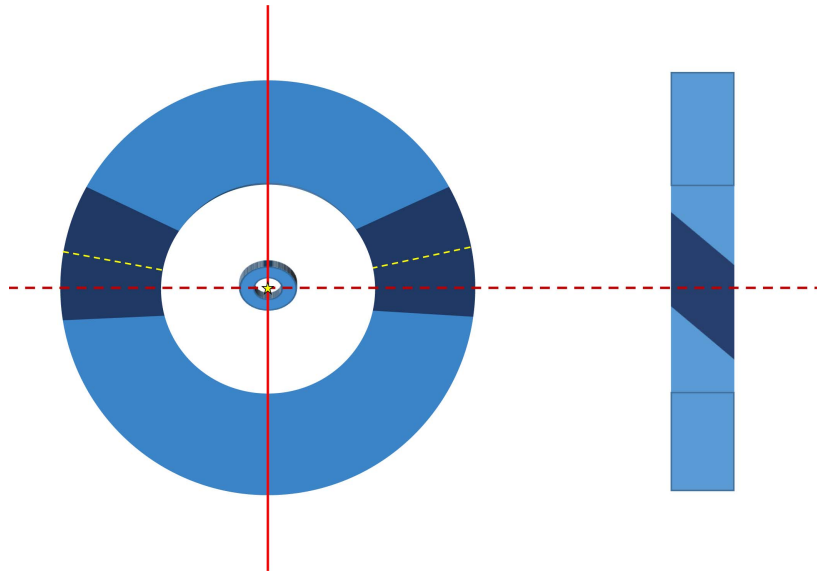


Figure 10. Face-on schematic of the outer disk (left) and vertical cross-section of the outer disk (right). The red dashed line represents the major axis of the inner disk, and the solid line denotes the vertical slice along which the cross section is produced. The inner disk is tilted, with the top edge closer to the observer in this schematic, and the dark regions represent the shadows it casts as it intersects the light coming from the central star (represented by the yellow star). In the cross section we can see how the shadow is shifted vertically in the direction of the tilt of the inner disk. The face-on view of the outer disk shows how the center of these shadows (yellow dashed line) can be offset from the view of the observer. Because of this offset, the separation of the shadows will always be smaller than 180° on the side of the outer disk, corresponding to the tilt of the inner disk.

4. Discussion

4.1. Dropoff in Spiral Arm Intensity with Wavelength

We observed a dropoff in spiral arm intensity at longer wavelengths in SPHERE TI imagery, most prevalent in *K1* (Figure 1), which suggests that they consist of small compact grains. Although the gas-to-dust ratio in the disk of HD 100453 is low (Kama et al. 2016), no tail dominated by small dust grains is detected by *HST* ACS (Collins et al. 2009). The lack of a tail, as seen in HD 141569 (Konishi et al. 2016) and young debris disks, suggests that the gas-to-dust ratio is not low enough for radiation pressure to dominate. If gravitational interactions with the M-type companion are the source of the spiral arms, the small grains, which are more tightly coupled to the gas than the large grains, would be pulled more easily along with the gas and may lie in a slightly different plane than the rest of the disk. This could explain why the arms are bluer than the rest of the outer disk and why, according to Fung & Dong (2015), they appear to be almost face on. When coupled with the difference in optical depth between the arms and the ring of the outer disk, this suggests that there is a gradient in the particle size distribution of the disk.

4.2. Rejection of a Coplanar Disk System

A coplanar inner and outer disk cannot reproduce the shadows seen in the SPHERE and GPI data. From the shadow separation and comparison of model images to data we find a misaligned inner disk with $\Delta i = 45^\circ \pm 10^\circ$ and a rotation of the inner-disk major axis of $-40^\circ \pm 10^\circ$ with respect to the outer disk or $100^\circ \pm 10^\circ$ east of north. This disagrees with Lazareff et al. (2017), however, who find a major axis PA for the inner edge of the inner disk of $81^\circ \pm 1^\circ$ east of north. This measurement was found using simplified ellipse and ring models of the inner disk based on VLTI/PIONIER *H*-band data taken from 2012 December 19 to 2013 February 20.

4.3. Investigation into the Shadow Location Over Time

At this time, there has been no observed change in the shadow pattern over the ~ 11.5 months spanned by the SPHERE data taken by Wagner et al. (2015) and Bensity et al. (2017). There is the possibility, however, of a 19° change in major axis position angle between the measurements of Lazareff et al. (2017) and Wagner et al. (2015) that spans ~ 25 – 27 months. If this is a change in the major axis, it could be due to precession of the inner disk, orbital motion of material in the inner disk, or the discrepancy could be a warp between the shadowing structure and the inner region of the inner disk.

Although the cause of the misalignment between the inner and outer disk is unknown, it has been shown in β Pic (Lagrange et al. 2010) that a planet can warp the inner disk. If a planet did cause the misalignment of the inner disk in HD 100453, as suggested above, it would likely cause precession of the inner disk, and by extension, precession of the shadows. However, this precession would occur on a timescale on the order of 10^3 times the orbital timescale expected from Newtonian dynamics (Rawiraswattana et al. 2016). This suggests that we should not observe a change in the location of the shadows as a result of precession for timescales shorter than a decade. A change of $19^\circ \pm 10^\circ$ in ~ 25 – 27 months ($\sim 16^\circ \text{ yr}^{-1}$) is too large to be accounted for with precession and is therefore not the cause of the discrepancy.

The orbital radius of an object with this orbital motion would be ~ 10 au. This is much larger than the proposed outer radius of the inner disk and just outside the region excluded by speckle residuals in GPI data. The large radius and lack of any disk detection in GPI data suggest that this is also most likely not the cause of the discrepancy between major axis PAs.

This leaves us with a warp between the inner region of the inner disk (traced by VLTI/PIONIER) and a shadowing region farther out. Although this cannot be ruled out using existing GPI or SPHERE data, *N*-band measurements using VLTI/

MATISSE would allow for the angular resolution necessary to detect any difference in the inner and outer portions of the inner disk.

4.4. Frequency of Transitional Disks with Misaligned Inner Disks

To date, 3 of the 14, that is $\sim 21\%$, transitional disks with published images have exhibited these shadows, which suggests that the shadows are not uncommon. The origin of the shadows is still under debate, however. Suggested causes include stellar magnetic activity (Pfeifer & Dong 2004), perturbation by the binary companion (Martin et al. 2014), and an unseen planet on an inclined orbit (Mouillet et al. 1997). However, magnetic field strengths in Herbig stars like HD 100453A are smaller, ~ 100 G (Hubrig et al. 2015), than the magnetic fields required for disk misalignment, $\sim 10^3$ G (Pfeifer & Dong 2004). A close binary system can cause a misaligned inner disk, but Collins et al. (2009) did not observe a strong X-ray source at the location of HD 100453A, which would be indicative of another M-type companion, and brighter stars would be visible in the SED. Alternatively, a wide binary system, where the companion lies outside of circumstellar disk (as in the case of HD 100453), can also cause misaligned disks. However, this causes a high outer-disk eccentricity at higher misinclinations (Martin et al. 2014), which is not seen here. The possibility of an unseen planet, however, makes HD 100453 a promising candidate for future planet searches (Gratia & Fabrycky 2016). To date, no radial velocity measurements have been taken for the star with the intent of planet detection, however. In addition, this system resembles β Pic in having a two-belt architecture and a misaligned inner disk, indicating that the similar structure in young debris disks is most likely inherited from the transitional disk phase.

5. Conclusions

We have carried out GPI PI imaging of HD 100453 in Y , J , and $K1$ bands and have examined the circumstellar disk using these data, the SED, and archival SPHERE TI imagery. With the help of the Monte Carlo radiative transfer code HOCHUNK3D, we generated models that allowed us to probe the inner and outer-disk morphology and make several testable predictions about the structure of the disk. Our conclusions are as follows.

1. The circumstellar disk of HD 100453 contains an inner disk that SED fitting suggests extends from 0.13 to 1 au, followed by a large radial gap (1–18 au) and an outer disk (18–39 au).
2. The outer disk is red in TI imagery, with $\frac{f_{\text{disk}}}{f_{\text{total}}} = 0.018 \pm 0.002$ in J band and $\frac{f_{\text{disk}}}{f_{\text{total}}} = 0.025 \pm 0.002$ in H band. This is similar in disk color to HR 4796, HD 169142, and 142527 (Schneider et al. 2009; Fukagawa et al. 2010), and is inconsistent with ISM-like grains at the disk surface. Its low gas-to-dust ratio (Kama et al. 2016) indicates that HD 100453 is evolving into a young debris disk.
3. Both TI and PI images exhibit azimuthally localized dark features at similar PAs. The size of the features is sufficiently large that any single body clearing them would be detected as a bright source (Janson et al. 2012). Given the sharpness and narrow size of the features and their consistent appearance in PI and TI light, we also

exclude inhomogeneities in grain properties. We therefore suggest that they are shadows cast by an optically thick misaligned inner disk.

4. An outer-disk inclination of 5° (Fung & Dong 2015) from face on is not supported by the data. In contrast, we measure an inclination of $25^\circ \pm 10^\circ$, in broad agreement with the 34° inclination reported in Wagner et al. (2015).
5. The degree of misalignment between the inner and outer disk can be determined using the separation of the shadows. We find this separation is best reproduced with a $\Delta i = 45^\circ \pm 10^\circ$, which also gives us the best fit to the NIR region of the SED.
6. Examination of the shadows can constrain the thickness of the inner disk. As the inner-disk thickness increases the width of the shadows, it causes also increase.
7. There is a difference in the color of the spiral arms and the rest of the outer disk. This suggests that they are most likely made of small grains that couple to gas more easily and are separated from the outer disk through interaction with the M-type companion.
8. There is a discrepancy of $\sim 19^\circ$ between the major axis PA for the inner disk found by Lazareff et al. (2017) and the one found in our study. Because of the long timescale required for precession and the lack of a visible blob at 10 au, we suggest that the cause of this discrepancy is a warp between the inner portion of the inner disk and an outer shadowing portion.

We have shown that shadow morphology and location constrain both the thickness and orientation of the inner disk as well as the flaring of the outer disk. This offers an independent means of measuring structure in transitional disks. In addition, the possibility of differences between the inner and outer edges of the inner disk is intriguing and should be investigated further. Predictions of the shadowing model will be tested for this and other Herbig Ae/Be stars with VLTI/MATISSE and other interferometric instruments in the future.

Based in part on data obtained at the Gemini Observatory via the time exchange program between Gemini and the Subaru Telescope (GS-2015A-C-1). The Gemini Observatory is operated by the Association of Universities for Research in Astronomy, Inc., under a cooperative agreement with the NSF on behalf of the Gemini partnership: the National Science Foundation (United States), the National Research Council (Canada), CONICYT (Chile), Ministerio de Ciencia, Tecnología e Innovación Productiva (Argentina), and Ministério da Ciência, Tecnologia e Inovação (Brazil). M.T. is partly supported by JSPS KAKENHI 2680016. C.A.G. is supported under NASA Origins of Solar Systems Funding via NNG16PX39P. Y.H. is supported by Jet Propulsion Laboratory, California Institute of Technology under a contract from NASA. M.S. is supported by NASA Exoplanet Research Program NNX16AJ75G. J.K. acknowledges support from Philip Leverhulme Prize (PLP-2013-110, PI: Stefan Kraus). S.K. acknowledges support from an ERC Starting Grant (Grant Agreement No. 639889). We also thank the referee for their comments and suggestions which added clarity to this paper.

References

- Andrews, S. M., Wilner, D. J., Zhu, Z., et al. 2016, *ApJL*, **820**, 2
 Apai, D., Schneider, G., Grady, C., et al. 2015, *ApJ*, **800**, 136
 Bessy, M., Stolker, T., Pohl, A., et al. 2017, *A&A*, **597**, A42
 Birnstiel, T., Andrews, S. M., & Ercolano, B. 2012, *A&A*, **544A**, 79B

- Brott, I., & Hauschildt, P. H. 2005, in ESA Spec. Publ. 576, The Three-Dimensional Universe with Gaia, ed. C. Turon, K. S. O’Flaherty, & M. A. C. Perryman (Noordwijk: ESA), 565
- Chen, X. P., Henning, T., van Boekel, R., & Grady, C. A. 2006, *A&A*, 445, 331
- Chiang, E. I., & Goldreich, P. 1997, *ApJ*, 490, 368
- Collins, K. A., Grady, C. A., Hamaguchi, K., et al. 2009, *ApJ*, 697, 557
- Cutri, R. M., Skrutskie, M. F., Van Dyk, S., et al. 2003, *yCat*, II/246, 0
- Dominik, C., Dullemond, C. P., Waters, L. B. F. M., & Walch, S. 2003, *A&A*, 398, 607
- Dong, R., Zhu, Z., Fung, J., et al. 2015, *ApJL*, 815, 1
- Dullemond, C. P., & Dominik, C. 2004a, *A&A*, 417, 159
- Dullemond, C. P., & Dominik, C. 2004b, *A&A*, 421, 1075
- Fukagawa, M., Tamura, M., Itoh, Y., et al. 2010, *PASJ*, 62, 347
- Fung, J., & Dong, R. 2015, *ApJ*, 815, 21
- Gaia Collaboration 2016, *yCat*, Gaia DR1
- Girard, J., Wahhaj, Z., Vigan, A., et al. 2016, PDM-ESO-254263 VLT-MAN-SPH-14690-0430, Very Large Telescope SPHERE User Manual, <https://www.eso.org/sci/facilities/paranal/instruments/sphere/doc.html>
- Gratia, P., & Fabrycky, D. 2016, arXiv:1607.08630
- Greaves, J. S., Kennedy, G. M., Thureau, N., et al. 2014, *MNRAS*, 438, L31
- Guimarães, M. M., Alencar, S. H. P., Corradi, W. J. B., & Vieira, S. L. A. 2006, *A&A*, 457, 581
- Hamilton, D. P., & Burns, J. B. 1992, *Icar*, 96, 43
- Hartmann, L., Calvet, N., Gullbring, E., & D’Alessio, P. 1998, *ApJ*, 495, 385
- Hubrig, S., Carroll, T. A., Schöller, M., & Ilyin, I. 2015, *MNRAS*, 449, 118
- Janson, M., Jayawardhana, R., Girard, J., et al. 2012, *ApJL*, 758, L2
- Kama, M., Bruderer, S., Carney, M., et al. 2016, *A&A*, 588, A108
- Khalafinejad, S., Maaskant, K. M., Marinas, N., & Tielens, A. G. G. M. 2016, *A&A*, 587, A62
- Konishi, M., Grady, C. A., Schneider, G., et al. 2016, *ApJL*, 818, 2
- Lagrange, A. M., Bonnefoy, M., Chauvin, G., et al. 2010, *Sci*, 329, 5987
- Lazareff, B., Berger, J.-P., Kluska, J., et al. 2017, *A&A*, 599A, 85
- Lucy, L. B. 1999, *A&A*, 344, 282
- Maaskant, K. M., Honda, M., Waters, L. B. F. M., et al. 2013, *A&A*, 555, A64
- Macintosh, B., Graham, J. R., Ingraham, P., et al. 2014, *PNAS*, 111, 35
- Maire, J., Perrin, M. D., Doyon, R., et al. 2010, *Proc. SPIE*, 7735, 773531
- Marino, S., Perez, S., & Casassus, S. 2015, *ApJL*, 198, 2
- Martin, R., Nixon, C., Lubow, S., et al. 2014, *ApJL*, 792, L33
- Meeus, G., Bouwman, J., Dominik, C., et al. 2002a, *A&A*, 392, 1039
- Meeus, G., Bouwman, J., Dominik, C., et al. 2002b, *A&A*, 402, 767
- Menu, J., van Boekel, R., Henning, Th., et al. 2015, *A&A*, 581, A107
- Mouillet, D., Larwood, J. D., Papaloizou, J. C. B., & Lagrange, A. M. 1997, *MNRAS*, 292, 896
- Mulders, G. D., Min, M., & Dominik, C. 2013, *A&A*, 549, A112
- Pascual, N., Montesinos, B., Meeus, G., et al. 2015, *A&A*, 585, A6
- Perrin, M. D., Maire, J., Ingraham, P., et al. 2014, *Proc. SPIE*, 9147, 91473J
- Pfeifer, H. P., & Dong, L. 2004, *ApJ*, 604, 766
- Rawiraswattana, K., Hubber, D. A., & Goodwin, S. P. 2016, *MNRAS*, 460, 4
- Schmid, H. M., Joos, F., & Tschan, D. 2006, *A&A*, 452, 657
- Schneider, G., Weinberger, A. J., Becklin, E. E., et al. 2009, *ApJ*, 137, 53
- Slettebak, A. 1966, *ApJ*, 145, 126S
- Stolker, T., Dominik, C., Avenhaus, H., et al. 2016, *A&A*, arXiv:1603.00481
- Wagner, K., Apai, D., Kasper, M., & Robberto, M. 2015, *ApJL*, 813, L2
- Whitney, B. A., Robitaille, T. P., Bjorkman, J. E., et al. 2013, *ApJS*, 207, 30
- Whitney, B. A., Wood, K., Bjorkman, J. E., & Wolff, M. 2003, *ApJ*, 591, 1049
- Wood, K., Wolff, M. J., Bjorkman, J. E., & Whitney, B. 2002, *ApJ*, 564, 887